

Mottness in two-dimensional van der Waals Nb_3X_8 monolayers ($\text{X}=\text{Cl}, \text{Br}, \text{and I}$)

Yi Zhang,¹ Yuhao Gu,² Hongming Weng,^{2,*} Kun Jiang,^{2,3,†} and Jiangping Hu^{2,4,‡}

¹Department of Physics, Shanghai University, Shanghai 200444, China

²Beijing National Laboratory for Condensed Matter Physics and Institute of Physics, Chinese Academy of Sciences, Beijing 100190, China

³School of Physical Sciences, University of Chinese Academy of Sciences, Beijing 100190, China

⁴Kavli Institute of Theoretical Sciences, University of Chinese Academy of Sciences, Beijing, 100190, China

(Dated: January 19, 2023)

We investigate strong electron-electron correlation effects on 2-dimensional van der Waals materials Nb_3X_8 ($\text{X}=\text{Cl}, \text{Br}, \text{I}$). We find that the monolayers Nb_3X_8 are ideal systems close to the strong correlation limit. They can be described by a half-filled single band Hubbard model in which the ratio between the Hubbard, U , and the bandwidth, W , $U/W \approx 5 \sim 10$. Both Mott and magnetic transitions of the material are calculated by the slave boson mean field theory. Doping the Mott state, a $d_{x^2-y^2} + id_{xy}$ superconducting pairing instability is found. We also construct a tunable bilayer Hubbard system for two sliding Nb_3X_8 layers. The bilayer system displays a crossover between the band insulator and Mott insulator.

INTRODUCTION

Strongly correlated materials display very rich intriguing physical properties [1]. For instance, the cuprates display antiferromagnetic Mott insulator, pseudogap, non-fermi liquid and many other unexpected phenomena besides their high-temperature superconductivity [2, 3]. To uncover the microscopic nature of these phenomena, different theoretical methods and numerical techniques, including resonating valence bond (RVB) [3], slave-boson mean-field [2], Gutzwiller approximation [3], dynamical mean-field theory (DMFT) [4], density matrix renormalization group (DMRG) [5] etc., have been developed. However, despite the tremendous efforts over the last forty years, strongly correlated models are barely solved. One of the major difficulties is that the correlated materials are often complicated by a strong interplay between spin, orbit, charge and lattice degree of freedoms [6–8]. For example, all five d-orbitals are intertwined in iron-based superconductors [9, 10]. Plain-vanilla systems with minimum parameters are highly desirable in strongly correlated materials. Twisted bilayer graphenes (TBG) with nearly vanishing bandwidth have been considered as ideal systems to investigate strong correlation in 2-dimensional (2D) van der Waals (vdW) materials [11–20]. But in reality, the low energy physics of TBG is not simple enough because of the interplay between layer, spin and valley [21–23].

Recently, Na_3Cl_8 has been shown to be a simple Mott insulator [24]. Using angle-resolved photoemission spectroscopy (ARPES), photoluminescence spectroscopy (PL) and DMFT calculations, a half-filled flat band with U around 0.8 eV~1.2 eV was observed in Na_3Cl_8 [24]. Additionally, a Josephson junction using Na_3Br_8 thin flake as a barrier also leads to a long-term chasing superconducting diode effect without the magnetic field, which is related to the strongly correlated nature of this material [25–33]. All these findings show the Nb_3X_8 ($\text{X}=\text{Cl}, \text{Br}, \text{I}$) may be an ideal platform to study correlation physics. In this work, we carry out a comprehensive investigation of the few layers Nb_3X_8 . Using the monolayer Nb_3X_8 , Mott insulator and magnetism at half-filling are found and the doping instability towards unconventional supercon-

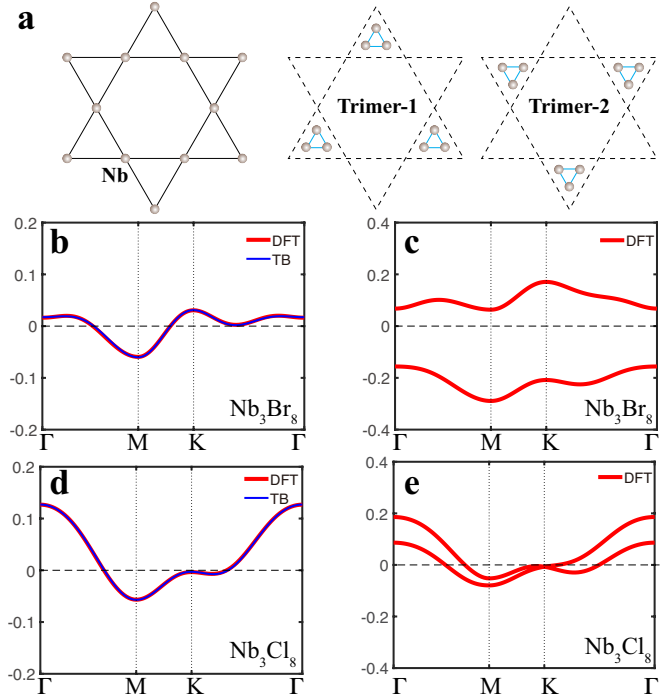


FIG. 1. **a**, The Nb Kagome lattice dominates the physics of Nb_3X_8 . The lattice is unstable towards two possible trimerization structures Trimer-1 and Trimer-2. **b**, The monolayer band structure (in unit of eV) of Nb_3Br_8 with DFT calculation (red line) and Wannierization fitting TB (blue line). **c**, The bilayer band structure of Nb_3Br_8 . **d**, The monolayer band structure of Nb_3Cl_8 . **e**, The bilayer band structure of Nb_3Cl_8 .

ductivity is discussed. Furthermore, a controllable bilayer Hubbard model is constructed by sliding two-layer Nb_3X_8 , where the crossover between the band insulator and Mott insulator takes place.

TIGHT-BINDING MODEL

We start from the non-interacting electronic structure of Nb_3X_8 using density functional theory (DFT) calculation and

Wannierization. The crystal structure of bulk Nb_3X_8 materials is a standard vdW structure by stacking Nb_3X_8 along the c direction [34–40]. Owing to the modern development in cleavage technique, reducing vdW materials down to a few layers and monolayer has now become a routine procedure [41, 42]. Hence, we will focus on the few-layer properties of Nb_3X_8 . Both the bulk and monolayer Nb_3X_8 electronic structure are dominated by the Nb 4d orbitals, where Nb atoms form a Kagome lattice as shown in Fig. 1a. However, the Nb Kagome lattice is not a stable structure with instability towards trimerization. Since the Kagome lattice is formed by two corner-sharing triangles, there are two ways of trimerization, Trimer-1 and Trimer-2, as illustrated in Fig. 1a. Because of this trimerization, the low energy theory of Nb_3X_8 is changed to a triangle lattice formed by Nb_3 clusters. For instance, the band structure of monolayer Nb_3Br_8 around Fermi level is simply one-band, as shown in Fig. 1b. And this band is formed by the $2a_1$ molecular orbital of Nb $4d_{z^2}$ trimers [24, 36, 38]. Therefore, the Kagome lattice is reduced to a triangle lattice with a doubled effective lattice constant. Taking into account the in-plane weak hopping of d_{z^2} , the bandwidth W is largely reduced down to 0.096 eV. Similarly, the band structure of monolayer Nb_3Cl_8 is also showing a one-band character with W around 0.2 eV, as plotted in Fig. 1d. The band structure of Nb_3I_8 is shown in the Supplemental Materials (SM) [43] (see also reference 1–3) with a bandwidth around 0.196 eV. Because of the similarity of these systems, we will take Nb_3Br_8 as an example in the following discussion.

Although the monolayer Nb_3Cl_8 and Nb_3Br_8 look similar, their ways of stacking are quite different. In Nb_3Br_8 , each Nb layer is trimerized into Trimer-1 while the Nb_3Cl_8 layers are trimerized into Trimer-1 and Trimer-2 alternatively. Hence, the Nb_3Br_8 bilayer is an insulator owing to the strong inter-layer hybridization of d_{z^2} orbitals, as plotted in Fig. 1c. On the other hand, the Nb_3Cl_8 bilayer is weakly coupled owing to the misalignment between two trimers, as shown in Fig. 1e.

Taking all above facts into account, we can construct the tight-binding (TB) model of Nb_3X_8 by Wannierization. The TB model of Nb_3X_8 monolayer can be written as

$$H_0 = \sum_{ij\sigma} t_{ij} c_{i,\sigma}^\dagger c_{j,\sigma} + h.c. - \mu \sum_{i\sigma} c_{i,\sigma}^\dagger c_{i,\sigma} \quad (1)$$

Here, we have included the hopping parameters up to the third-nearest-neighbours, with $t_1 = 5.4$ meV, $t_2 = 5.7$ meV, $t_3 = -6.3$ meV. As compared in Fig. 1b, this TB model can faithfully describe the Nb_3Br_8 . Then, the interaction term is added as the Hubbard model

$$H_I = U \sum_i n_{i\uparrow} n_{i\downarrow} \quad (2)$$

To treat Hubbard interaction non-perturbatively and study possible noncollinear magnetism in triangular lattice, we apply the $\text{SU}(2)$ spin-rotation invariant Kotliar-Ruckenstein slave boson theory [47] and represent the local Hilbert space by a spin-1/2 fermion f_σ and six bosons e , d , and p_μ ($\mu =$

0, 1, 2, 3) for empty, doubly-occupied, and singly occupied sites respectively [47–50]: $|0\rangle = e^\dagger |\text{vac}\rangle$, $|\uparrow\downarrow\rangle = d^\dagger f_\downarrow^\dagger f_\uparrow^\dagger |\text{vac}\rangle$, and $|\sigma\rangle = \frac{1}{\sqrt{2}} f_\sigma^\dagger p_\mu^\dagger \tau_{\sigma'\sigma}^\mu |\text{vac}\rangle$ where $\tau^{1,2,3}$ and τ^0 are Pauli and identity matrices [48–50]. Then, the hopping terms are renormalized to $\psi_i^\dagger g_i^\dagger g_j \psi_j$, where $\psi_i^\dagger = (f_{i\uparrow}^\dagger, f_{i\downarrow}^\dagger)$ and g_i is the renormalization factor defined in SM. The Hubbard interaction is written as $U \sum_i d_i^\dagger d_i$ with other local constraints discussed in SM. Then a mean-field solutions are obtained by boson condensation, which are equivalent to the Gutzwiller approximation [49].

The paramagnetic solution of the above model can be obtained by setting $p_{x/y/z}$ expectation values to zero. The metal-insulator transition [51] is hallmarked by chasing the doublon density $n_d = \langle d_i^\dagger d_i \rangle$, which is plotted in Fig. 2a. The n_d linearly decreases as U increases before reaching the Brinkman-Rice (BR) transition [52] at $U_{BR} = 158$ meV, where the renormalization factor g_i vanishes signaling a Mott transition. Since the Nb Hubbard U is expected to be 0.8–1.2 eV far beyond U_{BR} , the monolayer Nb_3X_8 lies deep inside the Mott phase. Hence, we need to consider the magnetic solution.

It is widely known that triangle lattice is a highly frustrated spin system with non-trivial magnetic solutions. The ground state of nearest-neighbor triangle Hubbard model at large U limit and Heisenberg model is $\sqrt{3} \times \sqrt{3}$ antiferromagnetism (AFM) with 120° ordering. The large U limit of Nb_3Br_8 can also be mapped to a highly frustrated $J_1 - J_2 - J_3$ Heisenberg model. Using slave boson mean-field, a 120° AFM order is found beyond the critical value $U_c = 93$ meV, as shown in Fig. 2b. Due to the limitation of mean-field theory, other exotic phases like the quantum spin liquids will be left to future work [53, 54].

RANDOM PHASE APPROXIMATION

Besides the Mott transition at half-filling, many interesting phenomena can show up by doping a Mott insulator, especially the unconventional superconductivity (SC). For example, a very rich phase diagram emerges for a broad doping range in the strongly correlated triangle lattice material Na_xCoO_2 with unconventional superconductivity [55, 56]. This superconductivity is widely believed to emerge from doping a Mott insulator with possible time reversal symmetry breaking [57, 58]. The high carrier tunability of 2D materials, through gating and ionic liquids etc., provides a direct way of doping this Mott insulator [21, 42]. To study the superconductivity instability, we apply a random-phase approximation (RPA) study by hole doping the system [59, 60]. Within the RPA approach, the spin susceptibility $\chi^s(\mathbf{q})$ and charge susceptibility $\chi^c(\mathbf{q})$ are given as:

$$\chi^{s/c}(\mathbf{q}) = \left[1 \mp \chi^0(\mathbf{q})U \right]^{-1} \chi^0(\mathbf{q}) \quad (3)$$

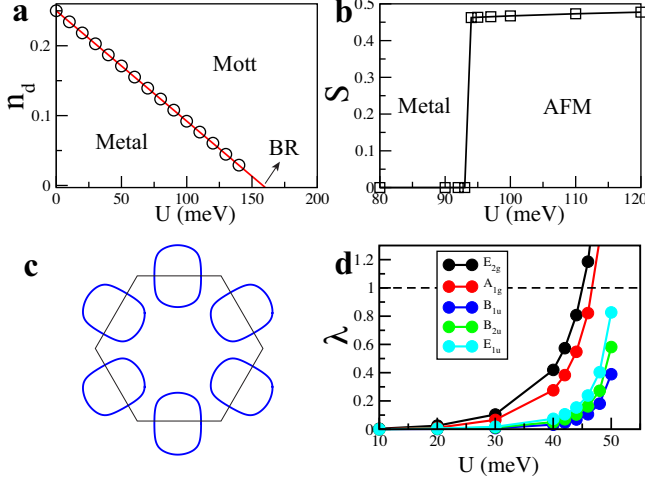


FIG. 2. **a**, Using slave boson mean field, the paramagnetic solution of monolayer Hubbard model is determined by the double occupancy n_d . The BR transition towards Mott occurs at $U_{BR} = 152$ meV. **b**, The magnetic expectation value S of monolayer Hubbard model with a phase transition towards $\sqrt{3} \times \sqrt{3}$ AFM at $U = 93$ meV. **c**, The Fermi surface of monolayer Nb_3Br_8 at hole doping $x = 0.1$. **d**, The various SC pairing instabilities determined by RPA approach. The leading instability is the E_{2g} channel (black line) or $d_{x^2-y^2} + id_{xy}$ channel. The subleading one is the A_{1g} s-wave channel (red line).

where the $\chi^0(\mathbf{q})$ is the noninteracting susceptibility. The effective pairing interaction $V(\mathbf{q})$ is constructed as

$$V(\mathbf{q}) = \frac{1}{4}\eta U^2 \chi^s(\mathbf{q}) - \frac{1}{8}U^2 \chi^c(\mathbf{q}) + \frac{1}{2}U \quad (4)$$

with $\eta = \frac{3}{2}$ for spin-singlet state and $\eta = -\frac{1}{2}$ for spin-triplet state. It governs the superconducting pairing instabilities through the linearized gap $\Delta(\mathbf{k})$ equation

$$\lambda \Delta(\mathbf{k}) = \frac{1}{N_s} \sum_{\mathbf{k}'} \frac{f(\varepsilon_{\mathbf{k}'}) - f(\varepsilon_{-\mathbf{k}'})}{\varepsilon_{\mathbf{k}'} - (-\varepsilon_{-\mathbf{k}'})} V(\mathbf{k} - \mathbf{k}') \Delta(\mathbf{k}') \quad (5)$$

where N_s is the number of sites, $\varepsilon_{\mathbf{k}}$ is the eigenband of Eq. 1, $f(\varepsilon)$ is the Fermi distribution function, and λ is the eigenvalue for the gap equation.

We solve the gap equation for the hole dope case with $x=0.1$, whose Fermi surface is shown in Fig. 3c and temperature $T=1$ meV for various values of U within a mesh of 60×60 \mathbf{k} points. The dominant pairing symmetry is determined by the gap function $\Delta(\mathbf{k})$ whose eigenvalue λ become unity firstly. By an approximate D_{6h} point group symmetry, the gap functions can be classified as its irreducible representations. In Fig. 2d, we plot several dominated gap function eigenvalues λ as a function of U . The leading SC instability is found to be E_{2g} channel, which corresponds to the $d_{x^2-y^2} + id_{xy}$ pairing symmetry. And this $d_{x^2-y^2} + id_{xy}$ pair breaks the time-reversal symmetry with the possible non-trivial topological property [58]. In the current case considered with hole-doping $x=0.1$, the system with a next nearest neighbor $d_{x^2-y^2} + id_{xy}$ pairing has Chern number ± 6 with more details of the calculation shown in SM [43]. The sub-leading instability is the

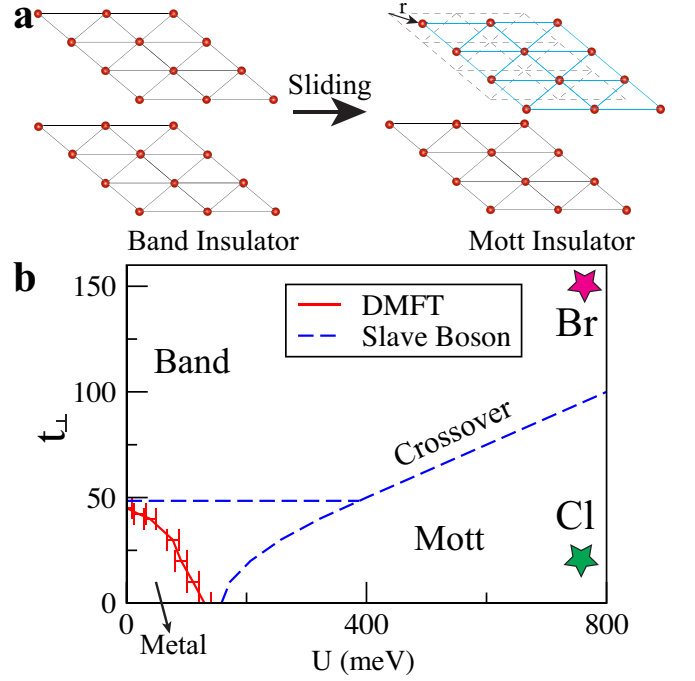


FIG. 3. **a**, The bilayer Nb_3Br_8 is used to construct a bilayer Hubbard model. By parallel sliding the top layer with distance r , the interlayer coupling t_{\perp} can be accurately adjusted. This sliding approach can be used to study the phase diagram of bilayer Hubbard model. **b**, The phase diagram of bilayer Hubbard model as function of U and t_{\perp} . The red line is the metal-insulator phase transition line determined by DMFT. There is a crossover between the band insulator limit and Mott insulator limit. We also use the slave boson mean field to find approximate boundary of BR transition (dashed lines), where the metal-insulator transition line is beyond this approach. The rough positions of bilayer Nb_3Br_8 and Nb_3Cl_8 are also labeled by pink star and green star respectively.

A_{1g} s-wave and other triplet channels are far away from spin singlet ones.

BILAYER HUBBARD MODEL

Besides the charge tunability, the flexibility of 2D materials and modern electronic techniques make the precise control and engineering of materials and devices possible. Successful engineering in small-angle twisted bilayer graphene provides a standard paradigm for this approach, where the bandwidth, interaction screening etc. can be adjusted [11, 12, 21]. Motivated by twisted bilayer graphene, we can also design the bilayer Nb_3X_8 . By introducing the layer index l , the bilayer system can be written as

$$H = \sum_{l=1,2} \sum_{i,j\sigma} t_{ij} c_{i,l\sigma}^{\dagger} c_{j,l\sigma} + \sum_{i\sigma} t_{\perp} c_{i,1\sigma}^{\dagger} c_{i,2\sigma} + h.c. + U \sum_{l,i} n_{i,l\uparrow} n_{i,l\downarrow} \quad (6)$$

where the t_{\perp} describes the interlayer coupling. Notice that the structure difference in Nb_3Cl_8 and Nb_3Br_8 materials leads to a huge difference in t_{\perp} as discussed above. Therefore, the

bilayer system can be tuned by sliding the top layer with distance r , as illustrated in Fig.3a. Then, the t_{\perp} can be approximately written as

$$t_{\perp}(r) = t_0 \exp(-r/r_0) \quad (7)$$

where r is defined as the in-plane distance reference to Nb_3Br_8 case in Fig.3a, $t_0 = 152$ meV is the interlayer coupling strength of Nb_3Br_8 and r_0 is a decay length by fitting the value at Nb_3Cl_8 , which is around $0.9 \sim 1.2\text{\AA}$.

Hence, the sliding bilayer system is one tunable system by controlling t_{\perp} , which can be used to study the bilayer Mott transition. In the $U = 0$ limit, the system undergoes a phase transition from metal to band insulator at large t_{\perp} . On the contrary, if t_{\perp} is zero, there is a Mott transition as discussed in the monolayer system. One interesting question arises: whether a Mott insulator and a band insulator are fundamentally different? This question has been widely discussed using both numerical and analytical approaches [8, 61–64]. Both crossover and phase transition between them have been identified [65–70]. The sliding design here may provide a way to settle down this debate.

Theoretically, we carry out a DMFT study of this model, where the spatial fluctuations of the self-energy are ignored with $\Sigma(k, i\omega_n) \approx \Sigma(i\omega_n)$ [4]. The Hubbard model is further mapped to an Anderson impurity model embedded in an interacting bath with the same self-energy [4]. Here, we use the hybridization expansion continuous-time quantum Monte Carlo package *i*QIST as the impurity solver [71, 72].

For the bilayer Hubbard model, the self-energy becomes a 2×2 matrix $\hat{\Sigma}(i\omega_n)$. To simplify the impurity calculation, it is more convenient to use the band basis. The band basis $a_{k,\alpha\sigma}$ ($\alpha = \pm$) is easily obtained as

$$a_{k,\pm\sigma} = \frac{1}{\sqrt{2}}(c_{k,1\sigma} \pm c_{k,2\sigma}) \quad (8)$$

with eigen-energy $E_{\pm}(k) = \epsilon(k) \pm t_{\perp}$ and $\epsilon(k)$ is monolayer band eigenfunction. The interaction terms are transformed into the multi-orbital Hubbard model as

$$\begin{aligned} H_I = & U_0 \sum_{i,\alpha} \hat{n}_{i,\alpha\uparrow} \hat{n}_{i,\alpha\downarrow} + U_v \sum_{i,\alpha\neq\alpha'} \hat{n}_{i,\alpha\uparrow} \hat{n}_{i,\alpha'\downarrow} \\ & - J \sum_{i,\alpha\neq\alpha'} (a_{i,\alpha\uparrow}^{\dagger} a_{i,\alpha'\downarrow}^{\dagger} a_{i,\alpha'\uparrow} a_{i,\alpha\downarrow} + a_{i,\alpha\uparrow}^{\dagger} a_{i,\alpha\downarrow}^{\dagger} a_{i,\alpha'\uparrow} a_{i,\alpha'\downarrow}) \end{aligned} \quad (9)$$

where $U_0 = U_v = J = \frac{U}{2}$. Then, the self-energy matrix becomes diagonal as

$$\hat{\Sigma}(i\omega_n) = \begin{pmatrix} \Sigma_+(i\omega_n) & 0 \\ 0 & \Sigma_-(i\omega_n) \end{pmatrix} \quad (10)$$

Using DMFT method, the phase diagram of bilayer Hubbard model is obtained, shown in Fig.3b. Besides the $U = 0$ transition and t_{\perp} transition discussed above, a metal-insulator transition line $U_c(t_{\perp})$ (red line in Fig.3(b)) is found by DMFT. As shown in Fig.3b, $U_c(0) = 158$ meV as the monolayer value. However, $U_c(t_{\perp})$ keeps decreasing as t_{\perp} increases before reaching the transition point at $t_{\perp} \approx 48\text{meV}$ and $U = 0$.

Besides the metal-insulator transition, no other phase transitions are found from the DMFT calculation. The transition between band insulator and Mott insulator is a crossover [66, 67]. This result shows there is no fundamental difference between band insulator and Mott insulator. To understand this crossover, we can study the single-site local interaction \hat{H}_{loc} problem with two electrons defined in SM. The eigenenergy and eigenfunctions for this problem are listed in TABLE I.

n	Eigenstate $ \Gamma_n\rangle$	E_{Γ_n}
1	$ \uparrow\downarrow, 0\rangle_a - \zeta 0, \uparrow\downarrow\rangle_a$	$U/2 - \sqrt{16t_{\perp}^2 + U^2}/2$
2	$ \uparrow, \downarrow\rangle_a - \downarrow, \uparrow\rangle_a$	0
3	$ \uparrow, \uparrow\rangle_a$	0
4	$ \downarrow, \downarrow\rangle_a$	0
5	$ \uparrow, \downarrow\rangle_a + \downarrow, \uparrow\rangle_a$	U
6	$ \uparrow\downarrow, 0\rangle_a + \zeta' 0, \uparrow\downarrow\rangle_a$	$U/2 + \sqrt{16t_{\perp}^2 + U^2}/2$

TABLE I. Eigenvectors $|\Gamma_n\rangle$ and their eigenenergy E_{Γ_n} for the single-site local interaction problem with two electrons. The eigenvectors here are defined in the band basis with subscript a. The first and second components of the state $|\text{1st}, \text{2nd}\rangle_a$ stand for the a_- and a_+ electrons respectively. We also drop out the normalization factor for convenience. Here, $\zeta = \frac{U}{\sqrt{16t_{\perp}^2 + U^2 + 4t_{\perp}}}$, $\zeta' = \frac{U}{\sqrt{16t_{\perp}^2 + U^2 - 4t_{\perp}}}$.

In TABLE I, we can find the lowest energy state of two electrons is E_{Γ_1} with mixing between $|\uparrow\downarrow, 0\rangle_a$ and $|0, \uparrow\downarrow\rangle_a$. Clearly, in the $U = 0$ limit, the ground state of the lattice model is the double occupied the $E_-(k)$ bands formed by the local eigenstate $|\uparrow\downarrow, 0\rangle_a$. This state is exactly the lowest energy state $|\Gamma_1\rangle$ at $U = 0$ limit. On the other hand, in the large U limit, $|\Gamma_1\rangle$ will be close to a local bound state $|\uparrow\downarrow, 0\rangle_a - |0, \uparrow\downarrow\rangle_a$. Switching back to the original c-basis with the two components of $|\uparrow, \downarrow\rangle_c$ corresponding to the electrons on the two layers respectively, this state becomes $|\uparrow, \downarrow\rangle_c - |\downarrow, \uparrow\rangle_c + \frac{\epsilon}{2t_{\perp}}(|\uparrow\downarrow, 0\rangle_c + |0, \uparrow\downarrow\rangle_c)$ with $\epsilon = E_{\Gamma_1}$. This approach is similar to the Heitler–London H_2 molecule theory, which leads to valence bond theory in chemistry [6, 7]. And this bound state forms the Mott insulator in the large U limit. Therefore, a band insulator will smoothly evolve into the Mott insulator without any phase transition [66, 67]. More than that, both the band insulator state and Mott insulator bound states are spin singlet states, which is consistent with experimental results in the bulk Nb_3X_8 [36, 38]. Moreover, we calculate the exact retarded Green's function in the atomic limit with more details shown in SM [43]. From the pole structure of the Green's function, we see that the interlayer hopping t_{\perp} splits the two Hubbard bands into four which is confirmed by the ARPES results [24].

In summary, we carry out a comprehensive study of the correlation physics in monolayer and bilayer Nb_3X_8 . The monolayer Nb_3X_8 is found to be a highly correlated narrow band system with U/W around 5~10. The Mott transitions are investigated by the slave-boson mean field. Because of the carrier tunability of 2D materials, the superconductivity instability is found to have $d_{x^2-y^2} + id_{xy}$ pairing. Additionally, by sliding two Nb_3X_8 layers, a tunable bilayer Hubbard

system is achieved. The bilayer model is further investigated by DMFT, where a crossover between the band insulator and Mott insulator is found. All these findings show that the 2-dimensional van der Waals Nb_3X_8 is a new platform for correlation physics. We hope our work gives a comprehensive understanding of this material and provides a new route toward correlation effects in 2D.

We thank Tian Qian, Z.-G. Chen for helpful discussions. This work is supported by the Ministry of Science and Technology (Grant No. 2017YFA0303100), National Science Foundation of China (Grant No. NSFC-11888101, No. NSFC-12174428), and the Strategic Priority Research Program of Chinese Academy of Sciences (Grant No. XDB28000000). Y.Z. is supported in part by NSF China Grant No. 12004383, No. 12074276 and No 12274279.

* hmweng@iphy.ac.cn

† jiangkun@iphy.ac.cn

‡ jphu@iphy.ac.cn

- [1] E. Dagotto, *Science* **309**, 257 (2005).
- [2] P. A. Lee, N. Nagaosa, and X.-G. Wen, *Rev. Mod. Phys.* **78**, 17 (2006).
- [3] P. W. Anderson, P. A. Lee, M. Randeria, T. M. Rice, N. Trivedi, and F. C. Zhang, *Journal of Physics: Condensed Matter* **16**, R755 (2004).
- [4] A. Georges, G. Kotliar, W. Krauth, and M. J. Rozenberg, *Rev. Mod. Phys.* **68**, 13 (1996).
- [5] U. Schöllwöck, *Rev. Mod. Phys.* **77**, 259 (2005).
- [6] P. Fazekas, *Lecture Notes on Electron Correlation and Magnetism* (WORLD SCIENTIFIC, Singapore, 1999).
- [7] A. Auerbach, *Interacting Electrons and Quantum Magnetism*, 1st ed. (Springer New York, New York, 1994).
- [8] S. S. Kancharla and E. Dagotto, *Phys. Rev. Lett.* **98**, 016402 (2007).
- [9] J. Paglione and R. L. Greene, *Nature Physics* **6**, 645 (2010).
- [10] X. Chen, P. Dai, D. Feng, T. Xiang, and F.-C. Zhang, *National Science Review* **1**, 371 (2014).
- [11] Y. Cao, V. Fatemi, A. Demir, S. Fang, S. L. Tomarken, J. Y. Luo, J. D. Sanchez-Yamagishi, K. Watanabe, T. Taniguchi, E. Kaxiras, R. C. Ashoori, and P. Jarillo-Herrero, *Nature* **556**, 80 (2018).
- [12] Y. Cao, V. Fatemi, S. Fang, K. Watanabe, T. Taniguchi, E. Kaxiras, and P. Jarillo-Herrero, *Nature* **556**, 43 (2018).
- [13] X. Lu, P. Stepanov, W. Yang, M. Xie, M. A. Amir, I. Das, C. Urgell, K. Watanabe, T. Taniguchi, G. Zhang, A. Bachtold, A. H. MacDonald, and D. K. Efetov, *Nature* **574**, 653 (2019).
- [14] A. L. Sharpe, E. J. Fox, A. W. Barnard, J. Finney, K. Watanabe, T. Taniguchi, M. A. Kastner, and D. Goldhaber-Gordon, *Science* **365**, 605 (2019).
- [15] Y. Jiang, X. Lai, K. Watanabe, T. Taniguchi, K. Haule, J. Mao, and E. Y. Andrei, *Nature* **573**, 91 (2019).
- [16] A. Kerelsky, L. J. McGilly, D. M. Kennes, L. Xian, M. Yankowitz, S. Chen, K. Watanabe, T. Taniguchi, J. Hone, C. Dean, A. Rubio, and A. N. Pasupathy, *Nature* **572**, 95 (2019).
- [17] Y. Xie, B. Lian, B. Jäck, X. Liu, C.-L. Chiu, K. Watanabe, T. Taniguchi, B. A. Bernevig, and A. Yazdani, *Nature* **572**, 101 (2019).
- [18] Y. Choi, J. Kemmer, Y. Peng, A. Thomson, H. Arora, R. Polski, Y. Zhang, H. Ren, J. Alicea, G. Refael, F. von Oppen, K. Watanabe, T. Taniguchi, and S. Nadj-Perge, *Nature Physics* **15**, 1174 (2019).
- [19] M. Yankowitz, S. Chen, H. Polshyn, Y. Zhang, K. Watanabe, T. Taniguchi, D. Graf, A. F. Young, and C. R. Dean, *Science* **363**, 1059 (2019).
- [20] M. Serlin, C. L. Tschirhart, H. Polshyn, Y. Zhang, J. Zhu, K. Watanabe, T. Taniguchi, L. Balents, and A. F. Young, *Science* **367**, 900 (2020).
- [21] E. Y. Andrei and A. H. MacDonald, *Nature Materials* **19**, 1265 (2020).
- [22] L. Balents, C. R. Dean, D. K. Efetov, and A. F. Young, *Nature Physics* **16**, 725 (2020).
- [23] J. Liu and X. Dai, *Nature Reviews Physics* **3**, 367 (2021).
- [24] S. Gao, S. Zhang, C. Wang, W. Tao, J. Liu, T. Wang, S. Yuan, G. Qu, M. Pan, S. Peng, Y. Hu, H. Li, Y. Huang, H. Zhou, S. Meng, L. Yang, Z. Wang, Y. Yao, Z. Chen, M. Shi, H. Ding, K. Jiang, Y. Li, Y. Shi, H. Weng, and T. Qian, arXiv e-prints, arXiv:2205.11462 (2022), arXiv:2205.11462 [cond-mat.str-el].
- [25] H. Wu, Y. Wang, Y. Xu, P. K. Sivakumar, C. Pasco, U. Filipozzi, S. S. P. Parkin, Y.-J. Zeng, T. McQueen, and M. N. Ali, *Nature* **604**, 653 (2022).
- [26] F. Ando, Y. Miyasaka, T. Li, J. Ishizuka, T. Arakawa, Y. Shiota, T. Moriyama, Y. Yanase, and T. Ono, *Nature* **584**, 373 (2020).
- [27] K. Misaki and N. Nagaosa, *Phys. Rev. B* **103**, 245302 (2021).
- [28] R. Wakatsuki, Y. Saito, S. Hoshino, Y. M. Itahashi, T. Ideue, M. Ezawa, Y. Iwasa, and N. Nagaosa, *Science Advances* **3**, e1602390 (2017).
- [29] Y. Tokura and N. Nagaosa, *Nature Communications* **9**, 3740 (2018).
- [30] J. Hu, C. Wu, and X. Dai, *Phys. Rev. Lett.* **99**, 067004 (2007).
- [31] N. F. Q. Yuan and L. Fu, *Proceedings of the National Academy of Sciences* **119**, e2119548119 (2022).
- [32] M. Davydova, S. Prembabu, and L. Fu, *Science Advances* **8**, eabo0309 (2022).
- [33] Y. Zhang, Y. Gu, P. Li, J. Hu, and K. Jiang, *Phys. Rev. X* **12**, 041013 (2022).
- [34] H. Schäfer and H. Schnering, *Angewandte Chemie* **76**, 833 (1964).
- [35] G. J. Miller, *Journal of Alloys and Compounds* **217**, 5 (1995).
- [36] J. P. Sheckelton, K. W. Plumb, B. A. Trump, C. L. Broholm, and T. M. McQueen, *Inorg. Chem. Front.* **4**, 481 (2017).
- [37] C. M. Pasco, I. El Baggari, E. Bianco, L. F. Kourkoutis, and T. M. McQueen, *ACS Nano* **13**, 9457 (2019).
- [38] Y. Haraguchi, C. Michioka, M. Ishikawa, Y. Nakano, H. Yamochi, H. Ueda, and K. Yoshimura, *Inorganic Chemistry* **56**, 3483 (2017).
- [39] J. Yoon, E. Lesne, K. Sklarek, J. Sheckelton, C. Pasco, S. S. P. Parkin, T. M. McQueen, and M. N. Ali, *Journal of Physics: Condensed Matter* **32**, 304004 (2020).
- [40] Z. Sun, H. Zhou, C. Wang, S. Kumar, D. Geng, S. Yue, X. Han, Y. Haraguchi, K. Shimada, P. Cheng, L. Chen, Y. Shi, K. Wu, S. Meng, and B. Feng, *Nano Letters* **22**, 4596 (2022).
- [41] K. S. Novoselov, A. K. Geim, S. V. Morozov, D. Jiang, Y. Zhang, S. V. Dubonos, I. V. Grigorieva, and A. A. Firsov, *Science* **306**, 666 (2004).
- [42] A. K. Geim and K. S. Novoselov, *Nature Materials* **6**, 183 (2007).
- [43] Technical details are provided in the Supplemental Materials.
- [1] G. Kresse and J. Furthmüller, *Computational Materials Science* **6**, 15 (1996).
- [2] G. Kresse and D. Joubert, *Phys. Rev. B* **59**, 1758 (1999).
- [3] J. P. Perdew, K. Burke, and M. Ernzerhof, *Phys. Rev. Lett.* **77**, 3865 (1996).
- [47] G. Kotliar and A. E. Ruckenstein, *Phys. Rev. Lett.* **57**, 1362

- (1986).
- [48] T. Li, P. Wölfle, and P. J. Hirschfeld, *Phys. Rev. B* **40**, 6817 (1989).
- [49] R. Frésard and P. Wölfle, *International Journal of Modern Physics B* **06**, 685 (1992).
- [50] K. Jiang, S. Zhou, and Z. Wang, *Phys. Rev. B* **90**, 165135 (2014).
- [51] M. Imada, A. Fujimori, and Y. Tokura, *Rev. Mod. Phys.* **70**, 1039 (1998).
- [52] W. F. Brinkman and T. M. Rice, *Phys. Rev. B* **2**, 4302 (1970).
- [53] Z. Zhu and S. R. White, *Phys. Rev. B* **92**, 041105 (2015).
- [54] Y. Iqbal, W.-J. Hu, R. Thomale, D. Poilblanc, and F. Becca, *Phys. Rev. B* **93**, 144411 (2016).
- [55] K. Takada, H. Sakurai, E. Takayama-Muromachi, F. Izumi, R. A. Dilanian, and T. Sasaki, *Nature* **422**, 53 (2003).
- [56] M. L. Foo, Y. Wang, S. Watauchi, H. W. Zandbergen, T. He, R. J. Cava, and N. P. Ong, *Phys. Rev. Lett.* **92**, 247001 (2004).
- [57] Q.-H. Wang, D.-H. Lee, and P. A. Lee, *Phys. Rev. B* **69**, 092504 (2004).
- [58] S. Zhou and Z. Wang, *Phys. Rev. Lett.* **100**, 217002 (2008).
- [59] Y. Yanagi, Y. Yamakawa, and Y. Ōno, *Journal of the Physical Society of Japan* **77**, 123701 (2008).
- [60] S. Graser, T. A. Maier, P. J. Hirschfeld, and D. J. Scalapino, *New Journal of Physics* **11**, 025016 (2009).
- [61] A. P. Kampf, M. Sekania, G. I. Japaridze, and P. Brune, *Journal of Physics: Condensed Matter* **15**, 5895 (2003).
- [62] C. D. Batista and A. A. Aligia, *Phys. Rev. Lett.* **92**, 246405 (2004).
- [63] A. Garg, H. R. Krishnamurthy, and M. Randeria, *Phys. Rev. Lett.* **97**, 046403 (2006).
- [64] N. Paris, K. Bouadim, F. Hebert, G. G. Batrouni, and R. T. Scalettar, *Phys. Rev. Lett.* **98**, 046403 (2007).
- [65] G. Moeller, V. Dobrosavljević, and A. E. Ruckenstein, *Phys. Rev. B* **59**, 6846 (1999).
- [66] A. Fuhrmann, D. Heilmann, and H. Monien, *Phys. Rev. B* **73**, 245118 (2006).
- [67] S. S. Kancharla and S. Okamoto, *Phys. Rev. B* **75**, 193103 (2007).
- [68] M. Sentef, J. Kuneš, P. Werner, and A. P. Kampf, *Phys. Rev. B* **80**, 155116 (2009).
- [69] H. Lee, Y.-Z. Zhang, H. O. Jeschke, and R. Valentí, *Phys. Rev. B* **89**, 035139 (2014).
- [70] M. Gall, N. Wurz, J. Samland, C. F. Chan, and M. Köhl, *Nature* **589**, 40 (2021).
- [71] E. Gull, A. J. Millis, A. I. Lichtenstein, A. N. Rubtsov, M. Troyer, and P. Werner, *Rev. Mod. Phys.* **83**, 349 (2011).
- [72] L. Huang, Y. Wang, Z. Y. Meng, L. Du, P. Werner, and X. Dai, *Computer Physics Communications* **195**, 140 (2015).

Supplemental Material: Mottness in two-dimensional van der Waals Nb₃X₈ monolayers (X=Cl, Br, and I)

COMPUTATIONAL DETAILS OF THE FIRST-PRINCIPLE CALCULATION

Our density functional theory (DFT) calculation is performed by Vienna ab initio simulation package (VASP) code [S1] with the projector augmented wave (PAW) method [S2]. The Perdew-Burke-Ernzerhof (PBE) [S3] exchange-correlation functional is used in our calculation. The kinetic energy cutoff is set to be 600 eV for the expanding the wave functions into a plane-wave basis. The energy convergence criterion is 10^{-7} eV and the Γ -centered \mathbf{k} -mesh is $12 \times 12 \times 2$. The monolayer Nb₃X₈ (X=Cl,Br,I) is fully relaxed with built-in 40 Å thick vacuum layer while forces are minimized to less than 0.001 eV/Å. The hopping parameters of tight-binding models are fitted from DFT-calculated band structures of monolayer Nb₃X₈. The band structure of Nb₃Cl₈ and Nb₃Br₈ are already shown in Fig.1 of the main text and the band structure of Nb₃I₈ is shown in Fig. S1.

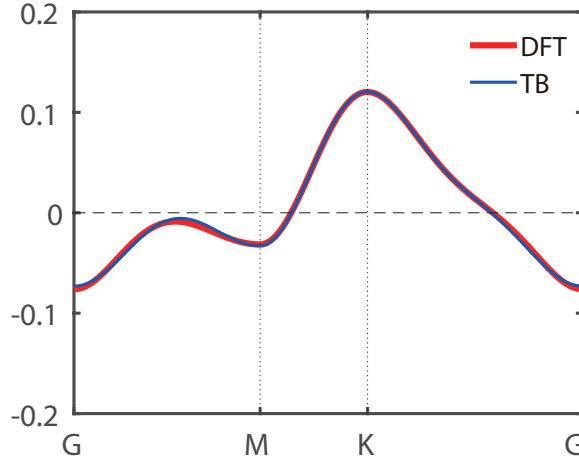


FIG. S1. The monolayer band structure of Nb₃I₈ with DFT calculation (red line) and Wannierization fitting TB (blue line) with the bandwidth around 0.196 eV.

LOCAL INTERACTION PROBLEM FOR THE BILAYER HUBBARD MODEL

The crossover between band insulator and Mott insulator can be understood from the local site problem of two electrons. The local Hamiltonian for the single site model can be written as

$$\hat{H}_{loc} = \begin{pmatrix} 0 & & & & & & & & \\ & U_v & -J & & & & & & \\ & -J & U_v & & & & & & \\ & & & 0 & & & & & \\ & & & & -2t_{\perp} + U_0 & J & & & \\ & & & & J & 2t_{\perp} + U_0 & & & \end{pmatrix} \begin{array}{l} |\uparrow, \uparrow\rangle_a \\ |\uparrow, \downarrow\rangle_a \\ |\downarrow, \uparrow\rangle_a \\ |\downarrow, \downarrow\rangle_a \\ |\uparrow\downarrow, 0\rangle_a \\ |0, \uparrow\downarrow\rangle_a \end{array} \quad (\text{S1})$$

in the 2-electron band basis $|\uparrow, \uparrow\rangle_a, |\uparrow, \downarrow\rangle_a, |\downarrow, \uparrow\rangle_a, |\downarrow, \downarrow\rangle_a, |\uparrow\downarrow, 0\rangle_a$, and $|0, \uparrow\downarrow\rangle_a$, which is defined as

$$\begin{cases} |\sigma, \sigma'\rangle_a = a_{+\sigma}^\dagger a_{-\sigma'}^\dagger |0\rangle \\ |\uparrow\downarrow, 0\rangle_a = a_{-\downarrow}^\dagger a_{-\uparrow}^\dagger |0\rangle \\ |0, \uparrow\downarrow\rangle_a = a_{+\downarrow}^\dagger a_{+\uparrow}^\dagger |0\rangle \end{cases} \quad (\text{S2})$$

Here, $U_v = J = U_0 = \frac{U}{2}$. The local interaction model in the original basis is

$$\hat{H}_{loc} = \begin{pmatrix} 0 & & & & \\ & 0 & t_{\perp} & t_{\perp} & \\ & & 0 & -t_{\perp} & -t_{\perp} \\ & & & 0 & \\ t_{\perp} & -t_{\perp} & U & 0 & \\ t_{\perp} & -t_{\perp} & 0 & U & \end{pmatrix} \begin{matrix} |\uparrow, \uparrow\rangle_c \\ |\uparrow, \downarrow\rangle_c \\ |\downarrow, \uparrow\rangle_c \\ |\downarrow, \downarrow\rangle_c \\ |\uparrow\downarrow, 0\rangle_c \\ |0, \uparrow\downarrow\rangle_c \end{matrix} \quad (S3)$$

in the 2-electron orbital basis $|\uparrow, \uparrow\rangle_c, |\uparrow, \downarrow\rangle_c, |\downarrow, \uparrow\rangle_c, |\downarrow, \downarrow\rangle_c, |\uparrow\downarrow, 0\rangle_c$, and $|0, \uparrow\downarrow\rangle_c$ defined as

$$\begin{cases} |\sigma, \sigma'\rangle_c = c_{2\sigma'}^{\dagger} c_{1\sigma}^{\dagger} |0\rangle \\ |\uparrow\downarrow, 0\rangle_c = c_{1\downarrow}^{\dagger} c_{1\uparrow}^{\dagger} |0\rangle \\ |0, \uparrow\downarrow\rangle_c = c_{2\downarrow}^{\dagger} c_{2\uparrow}^{\dagger} |0\rangle \end{cases} \quad (S4)$$

Diagonalizing \hat{H}_{loc} leads to the eigenvalues and eigenstates in TABLE I.

To see the difference between band and Mott insulator, we study the properties of the retarded Green's function in the two limiting cases. Deep in the Mott insulator case, we consider the atomic limit. In the zero temperature limit, the Lehmann representation of the Green's function leads to the local Green's function as

$$G_{\alpha\sigma, \alpha'\sigma'}^R(\omega) = \sum_n \left(\frac{\langle 0|a_{\alpha\sigma}|n\rangle \langle n|a_{\alpha'\sigma'}^{\dagger}|0\rangle}{\omega - \omega_{n0} + i\eta} + \frac{\langle 0|a_{\alpha'\sigma'}^{\dagger}|n\rangle \langle n|a_{\alpha\sigma}|0\rangle}{\omega + \omega_{n0} + i\eta} \right) \quad (S5)$$

where, $|n\rangle$ runs over all the eigenstates of the local Hamiltonian $\hat{H}_{loc} - \mu\hat{N}$, $|0\rangle$ is the ground state corresponding to $|\Gamma_1\rangle$ listed in TABLE I of the main text for the case with half filling and ω_{n0} corresponds to the energy difference between states $|n\rangle$ and $|0\rangle$ and η is an infinitesimal positive number. Here since $|0\rangle$ contains two electrons, $|n\rangle$ has to be the states with either one or three electrons. The local Hamiltonian in the 1-electron and 3-electron sectors are

$$\hat{H}_{loc} = \begin{pmatrix} -t_{\perp} & & & \\ & -t_{\perp} & & \\ & & t_{\perp} & \\ & & & t_{\perp} \end{pmatrix} \begin{matrix} |\uparrow, 0\rangle_a \\ |\downarrow, 0\rangle_a \\ |0, \uparrow\rangle_a \\ |0, \downarrow\rangle_a \end{matrix} \quad (S6)$$

and

$$\hat{H}_{loc} = \begin{pmatrix} U_0 + U_v - t_{\perp} & & & \\ & U_0 + U_v - t_{\perp} & & \\ & & U_0 + U_v + t_{\perp} & \\ & & & U_0 + U_v + t_{\perp} \end{pmatrix} \begin{matrix} |\uparrow\downarrow, \uparrow\rangle_a \\ |\uparrow\downarrow, \downarrow\rangle_a \\ |\uparrow, \uparrow\downarrow\rangle_a \\ |\downarrow, \uparrow\downarrow\rangle_a \end{matrix}. \quad (S7)$$

The calculated Green's function is diagonal in both spin and band basis and can be written as

$$G_{\alpha\sigma, \alpha\sigma}^R(\omega) = \frac{1}{1 + \zeta^2} \left[\frac{1}{\omega - (\bar{\alpha}t_{\perp} + E_{\alpha} - \mu) + i\eta} + \frac{\zeta^2}{\omega - (\bar{\alpha}t_{\perp} + E_{\bar{\alpha}} - \mu) + i\eta} \right] \quad (S8)$$

where, $\zeta = \frac{U}{\sqrt{16t_{\perp}^2 + U^2 + 4t_{\perp}}}$ and $E_{\pm} = \frac{1}{2}(U \pm \sqrt{16t_{\perp}^2 + U^2})$. Clearly, the Green's functions have four poles located at $\pm t_{\perp} + E_{\pm}$ for energy measured from the chemical potential μ , so that sufficient larger interlayer hopping t_{\perp} can split the two Hubbard bands into four which is confirmed by the ARPES experiment [S4]. On the other hand, in the band insulator limit with vanishing U , the Green's function is easy to get which can be written as

$$G_{\alpha\sigma, \alpha\sigma}^R(\omega) = \frac{1}{\omega - (\varepsilon_k + \alpha t_{\perp} - \mu) + i\eta} \quad (S9)$$

which only have two poles located at $\varepsilon_k \pm \alpha t_{\perp}$ for energy measured from μ . The difference in the number of poles of the Green's function can serve as an experimental feature to differentiate the two insulating states.

SLAVE BOSON APPROACH

In the Kotliar and Ruckenstein slave boson method, the local Hilbert space is represented by a spin-1/2 fermion f_σ and four slave bosons: e (holon), d (doublon), and p_σ , so that the empty state $|0\rangle = e^\dagger |vac\rangle$, the singly occupied state $|\sigma\rangle = p_{i,\sigma}^\dagger f_{i,\sigma}^\dagger |vac\rangle$ and the doubly occupied state $|\uparrow\downarrow\rangle = d_i^\dagger f_{i,\downarrow}^\dagger f_{i,\uparrow}^\dagger |vac\rangle$. The completeness of the local Hilbert space requires that the slave bosons satisfy the local constraints as,

$$Q_i = e_i^\dagger e_i + \sum_\sigma p_{i,\sigma}^\dagger p_{i,\sigma} + d_i^\dagger d_i - 1 = 0 \quad (\text{S10})$$

and the equivalence between the fermion and boson representation of the particle density requires the further constraint as,

$$Q_{i,\sigma} = p_{i,\sigma}^\dagger p_{i,\sigma} + d_i^\dagger d_i - f_{i,\sigma}^\dagger f_{i,\sigma} = 0, \quad (\text{S11})$$

Then the Hubbard model can be faithfully written as

$$H = \sum_{ij\sigma} t_{ij} g_{i,\sigma}^\dagger g_{j,\sigma} f_{i,\sigma}^\dagger f_{j,\sigma} + h.c. + U \sum_i d_i d_i - \mu \sum_i f_{i,\sigma}^\dagger f_{i,\sigma} - \sum_i \alpha_i Q_i - \sum_i \lambda_{i,\sigma} Q_{i,\sigma} \quad (\text{S12})$$

where the α_i and $\lambda_{i,\sigma}$ are Lagrange multipliers to enforce the constraints and $g_{i,\sigma}$ are the renormalization factors introduced for the hopping terms as

$$g_{i,\sigma} = L_{i,\sigma}^{-\frac{1}{2}} \left(e_i^\dagger p_{i,\sigma} + p_{i,\sigma}^\dagger d_i \right) R_{i,\sigma}^{-\frac{1}{2}} \quad (\text{S13})$$

with $L_{i,\sigma} = 1 - d_i^\dagger d_i - p_{i,\sigma}^\dagger p_{i,\sigma}$ and $R_{i,\sigma} = 1 - e_i^\dagger e_i - p_{i,\sigma}^\dagger p_{i,\sigma}$. The mean-field solution corresponds to condensing all the boson fields uniformly which are determined self consistently by minimizing the ground state energy $\langle H \rangle$ with respect to the condensed boson fields as well as the Lagrange multipliers $(e_i, d_i, p_{i,\sigma}, \alpha_i, \lambda_{i,\sigma}) = (e, d, p_\sigma, \alpha, \lambda_\sigma)$. For the uniformly condensed boson fields, the Hamiltonian Eq. S12 can be written in momentum space as

$$H = \sum_{\mathbf{k}\sigma} \varepsilon_{\mathbf{k}} g_{\sigma}^2 f_{\mathbf{k},\sigma}^\dagger f_{\mathbf{k},\sigma} + h.c. - (\mu + \lambda_\sigma) \sum_{\mathbf{k}} f_{\mathbf{k},\sigma}^\dagger f_{\mathbf{k},\sigma} + N_s U d^2 - N_s \lambda_\sigma (p_\sigma^2 + d^2) - N_s \alpha (e^2 + \sum_\sigma p_\sigma^2 + d_\sigma^2 - 1) \quad (\text{S14})$$

where

$$\begin{aligned} \varepsilon_{\mathbf{k}} = & 2t_1 (\cos(k_1) + \cos(k_2) + \cos(k_3)) + 2t_2 (\cos(k_1 + k_2) + \cos(k_2 + k_3) + \cos(k_3 - k_1)) \\ & + 2t_3 (\cos(2k_1) + \cos(2k_2) + \cos(2k_3)), \end{aligned} \quad (\text{S15})$$

with $k_1 = k_x$, $k_2 = \frac{1}{2}k_x + \frac{\sqrt{3}}{2}k_y$, $k_3 = -\frac{1}{2}k_x + \frac{\sqrt{3}}{2}k_y$ and

$$g_\sigma = \left(1 - d^2 - p_\sigma^2 \right)^{-\frac{1}{2}} (e p_\sigma + p_\sigma d) \left(1 - e^2 - p_\sigma^2 \right)^{-\frac{1}{2}}. \quad (\text{S16})$$

We solve for the boson field numerically in a mesh of 600×600 k points via minimizing the ground state energy $\langle H \rangle$ with respect to $(e, d, p_\sigma, \alpha, \lambda_\sigma)$ together with the chemical potential μ determined from the average particle density $n = (1/N_s) \sum_{i,\sigma} \langle f_{i,\sigma}^\dagger f_{i,\sigma} \rangle = 1 - x$. The determined phase diagrams for nonmagnetic and magnetic solutions are shown in Fig.2a,b of the main text.

TOPOLOGICAL PROPERTY OF THE d+id SUPERCONDUCTOR

As mentioned in the main text that the $d_{x^2-y^2} + id_{xy}$ pair breaks the time-reversal symmetry which can lead to possible non-trivial topological property. Here we take the $d_{x^2-y^2} + id_{xy}$ pairing symmetry with the next nearest neighbor pairing for the monolayer system as an example to show the non-trivial topological property. The total Hamiltonian of the superconductor can be written as

$$H = \sum_{\mathbf{k}\sigma} (\varepsilon_{\mathbf{k}} - \mu) c_{\mathbf{k}\sigma}^\dagger c_{\mathbf{k}\sigma} + \sum_{\mathbf{k}} (\Delta_{\mathbf{k}} c_{\mathbf{k}\uparrow}^\dagger c_{-\mathbf{k}\downarrow}^\dagger + h.c.) = \sum_{\mathbf{k}} h_{\mathbf{k}} \quad (\text{S17})$$

For the next nearest neighbor $d_{x^2-y^2} + id_{xy}$ pairing, the pairing potential has the form $\Delta_{\mathbf{k}} = \Delta_{\mathbf{k}}^\pm = \Delta_0 [\gamma_1(\mathbf{k}) \pm i\gamma_2(\mathbf{k})]$ with

$$\gamma_1(\mathbf{k}) = 2 \cos(k_2 + k_3) - \cos(k_1 + k_2) - \cos(k_1 - k_3) \quad (\text{S18})$$

$$\gamma_2(k) = -\sqrt{3} [\cos(k_1 - k_3) - \cos(k_2 + k_3)] \quad (\text{S19})$$

with $k_1 = k_x$, $k_2 = \frac{1}{2}k_x + \frac{\sqrt{3}}{2}k_y$, $k_3 = -\frac{1}{2}k_x + \frac{\sqrt{3}}{2}k_y$, which satisfies the relation $\Delta_{C_3(k)}^\pm = e^{\pm i\frac{2\pi}{3}} \Delta_k^\pm$ under the C_3 rotation. To determine the topological property of the superconductor, we calculate the Berry curvature of the system as

$$\Omega_n(k) = i \langle \nabla_k u_n(k) | \times | \nabla_k u_n(k) \rangle \quad (\text{S20})$$

where, $u_n(k)$ is the n th eigenstate of h_k , so that the Chern number can be determined as

$$C_n = \int \frac{dk}{2\pi} \Omega_n(k) \quad (\text{S21})$$

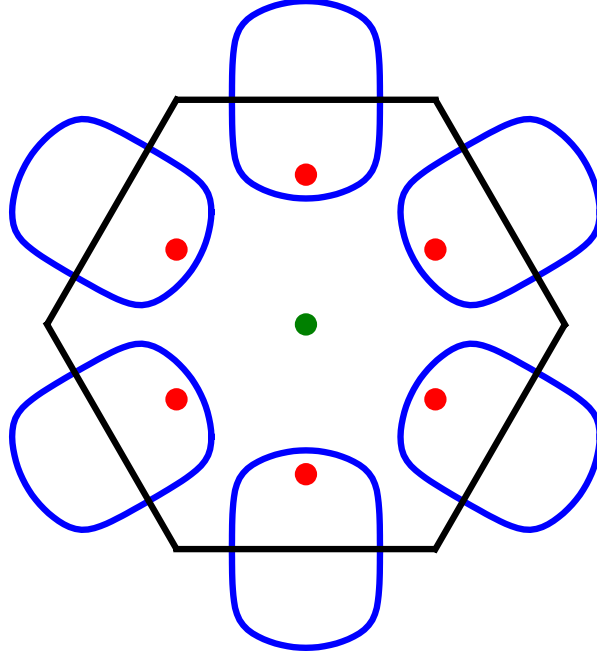


FIG. S2. Location of the poles (red and green dots) of the pairing potential Δ_k^\pm together with the Fermi surface (blue lines) of the mono layer system with hole doping $x=0.1$. Here, the black hexagon corresponds to the Brillouin zone.

For the monolayer system with hole doping $x=0.1$, we find the Chern number $C = \pm 6$ for Δ_k^\pm pairing. This can be understood from the poles of the pairing potential Δ_k^\pm that are enclosed by the Fermi surface of the normal state system [S5]. Here for the case we consider, the Fermi surface encloses six poles as shown in Fig S2, each of which contributes $\pm 2\pi$ of the Berry curvature, so that the total Chern number $C = \pm 6$ for Δ_k^\pm pairing superconductor.

* hmweng@iphy.ac.cn

† jiangkun@iphy.ac.cn

‡ jphu@iphy.ac.cn

[S1] G. Kresse and J. Furthmüller, *Comput. Mater. Sci.* **6**, 15 (1996).

[S2] G. Kresse and D. Joubert, *Phys. Rev. B* **59**, 1758 (1999).

[S3] J. P. Perdew, K. Burke, and M. Ernzerhof, *Phys. Rev. Lett.* **77**, 3865 (1996).

[S4] S. Gao, S. Zhang, C. Wang, W. Tao, J. Liu, T. Wang, S. Yuan, G. Qu, M. Pan, S. Peng, et al., arXiv e-prints arXiv:2205.11462 (2022), 2205.11462.

[S5] S. Zhou and Z. Wang, *Phys. Rev. Lett.* **100**, 217002 (2008).